Plasma Chemistry and Plasma Processing (2026) 46:84
https://doi.org/10.1007/s11090-026-10691-3

ORIGINAL PAPER

Controlling Reactivity at the Plasma-Liquid Interface: Applications to Remediation of PFAS in Water

Tiago C. Dias[1,5] · Jisu Jeon[2] · Stephen Olson[3] · Xuefei Qiu[4] · Selma Mededovic Thagard[4] · Mark J. Kushner[1]

Received: 21 March 2026 / Accepted: 25 June 2026

Abstract
Atmospheric pressure plasmas (APPs) can efficiently activate liquids by simultaneous delivery of electrons, ions, photons, and excited neutral species to the liquid surface. With the goal of controlling APP-liquid interactions, the impact of operational parameters on the formation and development of surface ionization waves (SIWs) was investigated with a two-dimensional numerical model, including the effects of the: (i) applied voltage pulse; (ii) liquid thickness (capacitance); (iii) liquid conductivity; and (iv) Ar/He gas mixture ratio. These parameters can be used to control the type and flux of reactive species arriving at the liquid surface, providing a means to tune the plasma-initiated chemistry. Higher voltages, thinner liquids, higher liquid conductivities, and helium-rich mixtures shift the system towards charge-dominated interfacial reactivity, whereas lower voltages, thicker liquids, lower conductivities, and argon-rich mixtures enhance photon-driven pathways. The ability to control reactivity delivered to the surface was applied to an investigation of APP destruction of per- and polyfluoroalkyl substances (PFAS) in water. Since long-chain PFAS preferentially accumulate at the gas–liquid interface, APPs that generate SIWs provide a targeted means of delivering reactive fluxes directly to these contaminants.

Keywords Atmospheric pressure plasma · Plasma-liquid interactions · Surface ionization waves · PFAS remediation

Introduction

Atmospheric pressure plasmas (APPs) are a versatile platform for activating liquids, simultaneously delivering fluxes of electrons, ions, photons, and a wide range of reactive neutral species to the liquid surface [1–4]. This capability has given rise to the field of plasma-driven solution electrochemistry (PDSE), which broadly refers to the delivery of plasma-generated species to an electrolytic solution (either isolated or grounded), with the goal of material synthesis or chemical conversion [5, 6]. A distinguishing feature of PDSE are the strong non-equilibrium conditions in the plasma – electron temperatures of several eV coexist with near-ambient gas temperatures, producing reactive fluxes at the plasma-liquid

Extended author information available on the last page of the article

Published online: 04 July 2026

interface that can exceed those of purely liquid-phase electrochemical systems by orders of magnitude. For example, PDSE has been successful in nanoparticle synthesis, where the gas-phase plasma serves as the reducing agent in a liquid electrolyte [7–10].

APPs that activate liquids have been broadly applied across several fields, including medicine [11, 12] and agriculture [13, 14], and have demonstrated high efficacy for water purification. This is particularly the case for the destruction of per- and polyfluoroalkyl substances (PFAS) in water, which are of increasing environmental concern. Long-chain PFAS (e.g., C8) contain a hydrophobic tail and tend to accumulate at the liquid surface behaving as surfactants. Since APPs often produce surface ionization waves (SIWs) that focus reactive particle fluxes at the plasma-liquid interface, they are well-suited for targeting and decomposing such surfactant-like contaminants [15–19].

Most APP-liquid applications use either a pulsed atmospheric pressure plasma jet (APPJ) or a DC glow discharge, where the latter typically requires a conductive solution and a counter electrode to sustain the DC current. However, pulsed APPJs are particularly promising, as the rapidly rising voltage generates large transient electric fields that exceed those in steady-state sources, producing time-averaged reactive fluxes greater than those by DC discharges [20, 21]. In pulsed APPJs interacting with liquids, the discharge typically forms a SIW that travels along the surface of the liquid. The development and propagation of the SIW arise from surface charging and electric-field enhancement at the plasma-liquid interface (where the liquid can be electrically viewed as a lossy dielectric) [10, 22, 23]. The electric field component parallel to the liquid surface sustains the SIW propagation and is generated by the surface charge deposited on the liquid. Once the SIW starts to propagate along the surface, charge separation develops at the wave front, forming a region of intense electric field that travels along the surface and initiates most of the chemical reactivity.

A key factor in optimizing APP-liquid interactions for specific applications is the control of the SIW properties. In this paper, we discuss results from a computational investigation of the propagation of pulsed APPJs onto liquid water sustained in argon/helium/water–vapor gas mixtures. We assess the impact of operational parameters of the plasma-liquid system on the formation and development of SIWs, including the: (i) amplitude of the voltage pulse applied to the powered electrode that initiates the gas-phase plasma; (ii) liquid thickness; (iii) liquid conductivity, adjusted by use of a NaCl solution; and (iv) argon/helium gas mixture ratio with a constant 0.5% water vapor impurity. The electrode voltage defines the bulk plasma and thus influences the charge delivered to the liquid surface. The liquid thickness is inversely proportional to the liquid electrical capacitance. Thinner liquids can sustain higher surface charge density, promoting stronger SIWs. The liquid conductivity, which governs dielectric losses, offers an alternative path for the discharge current through the liquid volume, affecting the horizontal current driven by the SIW across the liquid surface [24, 25]. Finally, the gas mixture directly influences the ratios of fluxes of reactive species reaching the plasma-liquid interface.

This study primarily focuses on configurations relevant to PFAS remediation in water. Due to the surfactant behavior of some long-chain PFAS, electron and photon fluences onto the liquid surface play a critical role in controlling the plasma-liquid reactivity and the success of remediation. As a result, particular attention is given to how these fluences vary under different operating conditions. The impact of these conditions and the fluxes onto the liquid they produce are evaluated by the rate of dissociation of the perfluorooctanoate anion (PFO^-, $C_8F_{15}O_2^-$), which resides in the liquid phase and is concentrated at the inter-

face. PFO^- originates from the dissociation of perfluorooctanoic acid (PFOA, $C_8HF_{15}O_2$) [26–28]. Although this investigation focuses on a single discharge pulse, while practical remediation of PFAS requires sustained processing, the reaction pathways identified here provide mechanistic guidance for the design of plasma-based remediation systems.

An overview of the numerical methods, simulation geometry, and chemical reaction mechanism used in this investigation are provided in Sect. "2". Results for the base case, consisting of a 115 ns, −15 kV discharge sustained in Ar/H_2O over a 2.4 mm of liquid water layer, with emphasis on plasma properties are presented in Sect. "3". The changes in plasma-liquid reactivity resulting from varying voltage, thickness, conductivity, and gas mixture (Ar/He content), are discussed in Sect. "4". The implications of these changes for PFO^- dissociation, along with an assessment of the dominant dissociation pathways, are discussed in Sect. "5". Concluding remarks are in Sect. "6".

Description of the Model and Conditions

Brief Overview of nonPDPSIM

The simulations in this investigation were performed using *nonPDPSIM*, a two-dimensional plasma hydrodynamics model executed on an unstructured mesh. *nonPDPSIM* has been described in detail elsewhere [29], and so only a brief overview is provided here. The model comprises several modules containing algorithms integrated using time-slicing techniques, which enable picosecond time steps resolving the discharge dynamics and several nanosecond time steps during the afterglow.

In the plasma transport module, Poisson's equation for electrical potential, continuity equations for charged species, and charge densities in and on materials, are concurrently solved using implicit methods. Charged particle fluxes are computed using a drift–diffusion approximation utilizing the Scharfetter-Gummel method. Secondary electron emission on all solid surfaces was included for incident positive ion species and photons, with constant emission coefficients of 0.25 and 0.01, respectively. Secondary electron emission on liquid surfaces was neglected here since it has been estimated by Delgado et al. [30] to have a probabilitysmaller than 10^{-5}. The divergence operators in these equations are discretized using the finite volume method.

Following the calculation of the electric potential and charge densities, the bulk electron temperature, T_e, is synchronously updated as a function of position by implicitly solving the electron energy conservation equation using a successive-over-relaxation (SOR) method. Rate and transport coefficients are obtained as functions of T_e by solving the stationary electron Boltzmann's equation over a range of reduced electric fields, E/N, and tabulating the results using T_e as the independent variable. These tables are updated during the simulation as the mole fractions of collision partners change. Separate tables are constructed for mesh zones with significantly different gas compositions.

The continuity equations for neutral species densities are solved under the assumption that individual neutral species diffuse within a single background fluid and may react with surfaces. These equations are also solved implicitly using a SOR method. The background neutral flow field is described by a modified version of the Navier–Stokes (NS) equations – continuity, momentum, and energy – using unsteady, compressible, implicit algorithms. The

formalism accounts for momentum transfer from electric-field-driven ions and electrons to the neutral fluid, Joule heating from ions, and energy release from reactions. However, momentum transfer and gas heating are not significant for the single-pulses investigated in this work. The integration of the NS equations is coupled to other modules using time-slicing techniques and, in this work, was updated every 1 ns.

The multi-phase (gas and liquid) capabilities of *nonPDPSIM* were employed in this investigation [10]. The shape of the gas–liquid interface is assumed to be static. Fluxes of neutral gas-phase species into and out of the liquid are limited by Henry's law equilibrium at the liquid surface, such that the flux of a gas phase species into the liquid goes to zero when the corresponding solvated species at the liquid surface reaches saturation. If the solvated species is supersaturated, the net flux at the boundary is from the liquid towards the gas phase, although we do not require that species at the surface be in a Henry's law equilibrium. Other processes such as reactions and rate of transport from the surface ultimately determine densities of species at the surface. For details on the numerical implementation of these interfacial fluxes, see Eqs. (1) and (2) of Ref. [10]. These Henry's law-based transport limits apply only to neutral species crossing the gas–liquid interface. Transport within the bulk gas and liquid phases, away from or towards the interface, is not otherwise constrained. All incident ions, electrons, and photons arriving at the gas–liquid interface are assumed to enter the liquid. The temperature of the liquid phase was maintained at 300 K.

Plasma-Surfactant Module

In this investigation, the powered electrode was pulsed negatively, and the liquid functionally serves as the anode. Prior to the surface of the liquid charging, electrons are accelerated into the solution, producing significant incident electron fluxes with energies of several eV. Upon reaching the liquid surface, these electrons can undergo inelastic collisions with liquid species before the electrons solvate, leading to the dissociation and ionization of surface resident molecules. Such electron-impact processes can be particularly relevant for long-chain PFAS remediation in water [15] as these species exhibit surfactant-like behavior. These processes are modeled in *nonPDPSIM* using the Plasma-Surfactant Module (PSM). The PSM first described in [10] was further developed in this work. For the PSM, the term *surfactant* is used broadly to denote any liquid-phase molecule residing at the surface, including water itself. To make clear the distinction between gas and liquid species, from this point on, the subscript "aq" refers to an aqueous or in-liquid species.

Surfactants in the liquid are hypothesized to react with gas phase species (electrons, ions, and neutrals) incident onto the liquid surface. The rates of these reactions differ from those of bulk liquid reactions as they directly rely on the flux of gas phase species to the liquid surface. Considering the unstructured numerical mesh, at the liquid phase mesh point i on the surface having neighboring mesh nodes j in the gas phase, the rate of reaction for process m ($\mathrm{cm^{-3}\ s^{-1}}$), resulting from the incident flux of gas phase species q is

$$R^{\mathrm{s}}_{imq} = \sum_{j}^{\mathrm{n}} \frac{A_{ji}\phi_{qji}\mathcal{N}_m\sigma^{\mathrm{eff}}_{qjm}}{V_i} \tag{1}$$

The sum is over the n gas phase mesh points that are neighbors of liquid node i. Here, s stands for surfactant rate contribution, ϕ_{qji} is the flux of species q from gas phase node j to liquid phase node i passing through the face of the liquid volume element having area A_{ji}, and V_i is the volume of the liquid cell. $\mathcal{N}_m$ is the surface density (cm^{-2}) of the liquid phase species for process m. The value of $\mathcal{N}_m$ is discussed below. (Note that in Eq. (3) in [10] the molar fraction should be replaced by the surface density. The surface density was properly accounted for in the model.)

$\sigma_{qjm}^{\text{eff}}$ is the effective cross section for species q reacting at node j for process m and is estimated as

$$\sigma_{qjm}^{\text{eff}} = \frac{k_{qjm}(T_{qj})}{v_{th,qj}} \tag{2}$$

where $k_{qjm}(T_{qj})$ is the rate coefficient at node j for species q and process m, and T_{qj} and $v_{\text{th},qj}$ are the temperature and the thermal speed of gas-phase species q arriving from node j to node i. The gas-phase rate coefficients are used to approximate the interactions between incident gas-phase species and surface-resident molecules. When computing the effective cross sections for each process m, the algorithm ensures that the total cross section describing the interaction between the incident species and the liquid species does not exceed the surface-site area occupied by the liquid molecule (A_s). For H_2O_{aq} molecules, the surface-site area is estimated from the total liquid density n_l as $A_{si}^{H_2O} = n_l^{-2/3} \approx 9.67 Å^2$. However, PFO^-_{aq} molecules are larger than H_2O_{aq}, thereby occupying a larger cross-sectional area [31]. Here, we assumed $A_{si}^{PFO} = 5A_{si}^{H_2O} \approx 48.3\ Å^2$. When the total cross section of a gas–liquid pair is limited to A_{si}, the renormalization ensures that the branching ratios for each process m are preserved. Under the conditions explored in this work, only some charge exchange processes require such a renormalization.

When the species at the liquid surface is not a surfactant (amphiphilic), the surface density $\mathcal{N}_m$ is estimated from the volumetric bulk density n_m (cm^{-3}):

$$\mathcal{N}_m^{\text{b}} = \frac{n_m}{n_l} n_l^{2/3} \tag{3}$$

In the case of surfactants, a monolayer of molecules accumulates at the liquid surface, leading to a larger surface density described by [32]:

$$\mathcal{N}_m^{\text{s}} = N_A \Gamma_{\max} \frac{c_m}{c_m + \beta} \tag{4}$$

where N_A is Avogadro's constant, $\Gamma_{\max}$ is the maximum surface excess (mol cm^{-2}), c_m is the bulk concentration (M ≡ mol/L), and β is the concentration at half saturation (M). $\Gamma_{\max}$ and β depend on the surfactant properties and can be obtained from experimental measurements reported in the literature. For $PFO(A)_{aq}$ [33], $\Gamma_{\max} \approx 5.3 \times 10^{-10}$ mol cm^{-2} and $\beta \approx 1.75 \times 10^{-4}$ M. Note that Eq. (4) is valid only for surfactant concentrations below the critical micelle concentration (CMC) [32]. For $PFO(A)_{aq}$, the CMC is 3460 ppm [34], while the PFO^-_{aq} concentration studied in this work is 1 ppm. For this concentration, the PFO^-_{aq}

surface density is $\approx 4.3 \times 10^{12}$ cm^{-2}. For more details on the surface excess of surfactant molecules, see Chapter 2-III of Rosen and Kunjappu [32] and Constanza et al. [34].

For the case of incident (hot) electrons, an additional rate component (R^{v}_{imq}) is included in the surfactant module to account for reactions occurring in the liquid volume, produced by electrons that do not react at the surface. With $q=e$ referring to the electron species,

$$R_{ime} = R^{\mathrm{s}}_{ime} + R^{\mathrm{v}}_{ime} = \sum_{j}^{\mathrm{n}} \frac{A_{ji}\phi_{eji}\sigma^{\mathrm{eff}}_{ejm}}{V_i} \left(\mathcal{N}_m + (1 - p_{eji}) n_m \lambda_{eji}\right) \tag{5}$$

where v stands for volumetric contribution, p_{eji} is the probability of an electron reacting at the surface, and λ_{eji} is the mean free path of the electron in the liquid. Both p_{eji} and λ_{eji} are calculated by summing over all possible inelastic processes. The additional volume contribution is not included for incident radicals or ions because the reactions of these species in the liquid volume can be adequately described through standard liquid-phase chemistry once solvation occurs. For incident hot electrons, however, the situation differs because the temperature of the electrons after solvation is much lower than that of the incident electrons, and the additional volume contribution from these highly reactive electrons would otherwise not be captured.

Reaction probabilities (or sticking coefficients) are commonly used to describe interactions of gas phase species with condensed phases (solids or liquids). These values can ultimately be derived from an effective cross section associated with a surface site. We opted to formalize plasma-surfactant reactions here using an effective cross section instead of the higher level reaction probability. The effective cross sections can be approximated from rate coefficients and enable addressing a liquid surface composed of an arbitrary number of species having any surface density. Surface reaction probabilities can be deduced from the product of the species surface density and the effective cross section.

The products of the plasma-surfactant processes are assumed to remain in the liquid phase, although the model permits them to return to the gas phase if necessary. In the particular case of plasma-based remediation of PFAS, experiments suggest that the majority of products remain in the liquid phase [35].

Photoabsorption Module

Radiation transport and photoabsorption are addressed in *nonPDPSIM* using a Green's function approach, as described in [29]. Here, we summarize the method and the modifications introduced to account for surfactant-like species at the gas–liquid interface. The photoabsorption source (cm^{-3} s^{-1}) for a process i at location $\vec{r}_j$ arises from the integral of photon emission from all other locations $\vec{r}_l$,

$$S_{Pi}(\vec{r}_j) = n_i(\vec{r}_j) \cdot \sum_k \sigma_{ik} A_k \int n_k(\vec{r}_l) G_{ljk}(\vec{r}_l, \vec{r}_j)\ \mathrm{d}^3\vec{r}_l \tag{6}$$

where σ_{ik} is the photoabsorption cross section of the process i for photons emitted by species k, and A_k is the emission frequency for the transition. G_{ljk} is the Green's function describing the relative flux of the photon emitted at $\vec{r}_l$ that survives to reach $\vec{r}_j$:

$$G_{ljk}(\vec{r}_l,\vec{r}_j)=\frac{\exp\left(-\int_{\vec{r}_l}^{\vec{r}_j}\sum_m \sigma_{mk}n_m(\vec{r}_p)\mathrm{d}\vec{r}_p\right)\cdot\left(1-\sum_m \sigma_{mk}\mathcal{N}_m\right)_{\mathrm{surf}}}{4\pi|\vec{r}_l-\vec{r}_j|^2} \tag{7}$$

where the integral in the exponent accounts for absorption of photon *k* by all absorbing species *m* with cross section σ_{mk} and number density n_{m}. The second term in the numerator is applied only if the path between $\vec{r}_l$ and $\vec{r}_j$ intersects a gas–liquid interface, in which case $\mathcal{N}_m$ denotes the surface density of the absorbing species evaluated at the intersection point. Generating G_{ljk} in the unstructured mesh is expensive due to the evaluation of the integral along the cord. For this reason, G_{ljk} is not recomputed unless the density of absorbers significantly changes.

For liquid cells at the gas–liquid interface, in addition to the volumetric photoabsorption source term given by Eq. (6), photoabsorption due to process *i* at the liquid surface is included as:

$$S_{Pi}(\vec{r}_j)|_{\mathrm{s}}=\frac{\mathcal{N}_i A_{\mathrm{s}}}{V_{\mathrm{s}}}\cdot\sum_k \sigma_{ik}A_k\int n_k(\vec{r}_l)G_{ljk}(\vec{r}_l,\vec{r}_j)\ \mathrm{d}^3\vec{r}_l \tag{8}$$

where A_{s} is the cell area at the gas–liquid interface, V_{s} is the cell volume, and $\mathcal{N}_i$ is the surface density at the interface.

Operating Conditions

The source geometry used in this work is shown in Fig. 1a. The two-dimensional (2D) Cartesian geometry implemented in *nonPDPSIM* is symmetric about the left-hand boundary. The APPJ source is positioned above the liquid and consists of a tungsten powered electrode, 1.2 mm in width, placed inside a glass tube with 2.4 mm inner width and 0.6 mm thick (relative permittivity $\varepsilon_{\mathrm{r}}=4$). The downstream ends of both the powered electrode and the glass tube are rounded. The distance between the tip of the powered electrode and the liquid surface is 5 mm. The region below the liquid and the entire right-hand side of the simulation domain are electrically grounded. The voltage applied to the powered electrode is varied from −12 kV to −18 kV (base case is −15 kV). The pulse length is 115 ns, linearly rising from 0 kV to the maximum (absolute) value over the first 5 ns and maintaining a constant value until 90 ns. The voltage then linearly ramps to zero over 15 ns. The liquid thickness was varied from 0.8 mm to 5.0 mm (base case is 2.4 mm). The depth of the simulation domain was set to 1 cm. This value does not influence the results, aside from setting a constant factor for the total number of particles collected on surfaces.

The mesh nodes and connectors are shown in Fig. 1b, where the mesh resolution varies between a minimum of 25 μm/cell near the powered electrode surface and maximum of 1.2 mm/cell far away from the liquid surface. The numerical mesh used for 2.4 mm liquid thickness consists of 16,010 total nodes, comprising 11,737 gas-phase nodes and 4,273 liquid-phase nodes.

The investigations presented here involve argon/helium gas mixtures containing a constant 0.5% water vapor impurity and liquid water with varying $NaCl_{aq}$ concentrations to adjust conductivity. (For reference, at 293 K, the saturated water vapor concentration in air is about 2.3%.) The geometry and operating conditions are designed to be broadly con-

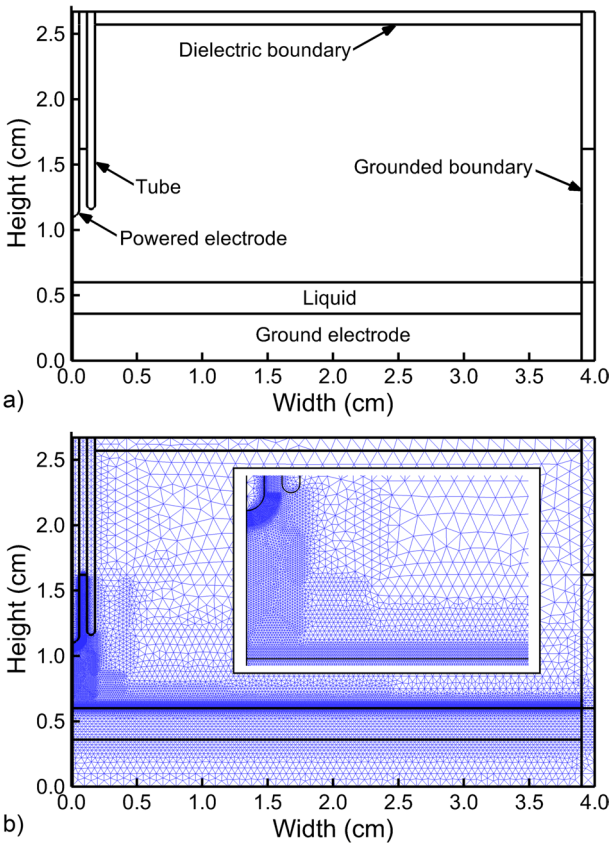

Fig. 1 Schematics of the (**a**) plasma-liquid geometry and (**b**) the numerical mesh for a liquid layer thickness of 2.4 mm

sistent with the experimental work of Mededovic-Thagard [15, 36, 37] on plasma-assisted PFAS remediation, in which water flows through a treatment chamber while argon is used as the working gas. In those systems, the argon stream is nominally saturated with water vapor due to evaporation from the liquid. Although *nonPDPSIM* is capable of simulating complex flow patterns, for simplicity a spatially uniform background gas composition was assumed prior to pulsing. The argon/helium ratio was varied from 1/0 to 0/1 while maintaining the same water vapor content. The base case corresponds to pure argon with water vapor. The $NaCl_{aq}$ concentration in the liquid was varied from 0.0 to 15.8 mM, corresponding to conductivities between 0.0 and 2.0 mS/cm (base case is 0.79 mM, 0.1 mS/cm) [38]. Due to the relatively low $NaCl_{aq}$ concentration, the salt is assumed to be fully dissociated into Na^{+}_{aq} and Cl^{-}_{aq}.

To assess the impact of plasma exposure on PFAS dissociation, 1 ppm of perfluorooctanoic acid ($PFOA_{aq}$, $C_8HF_{15}O_{2aq}$) was set in the bulk liquid. Values reported in the literature for the acid dissociation constant pK_a of $PFOA_{aq}$ range from −0.1 to 3.8 [26–28]. Using a pK_a of 3.8 for $PFOA_{aq}$ [26], corresponds to the limit of least dissociation. For these conditions more than 98% of the acid is deprotonated, leading to the formation of perfluorooctanoate anion (PFO^{-}_{aq}) and $H_3O^{+}_{aq}$ [39]. Accordingly, PFO^{-}_{aq} is treated as the sole PFAS aqueous species in this work.

Table 1 Species in the reaction mechanism

Gas phase charged	e, Ar^+, Ar_2^+, He^+, He_2^+, HeH^+, H^+, H^-, H_2^+, H_3^+, OH^+, OH^-, H_2O^+, H_3O^+, O^+, O^-, O_2^+, O_2^-, O_3^-, O_4^+
Gas phase neutral (ground)	Ar, He, H, H_2, OH, H_2O, HO_2, H_2O_2, O, O_2, O_3
Gas phase neutral (excited)	$Ar(4s^1s_5)$, $Ar(4s^1s_4)$, $Ar(4s^1s_3)$, $Ar(4s^1s_2)$, Ar(4p), Ar(4d), Ar_2*,$He(2s^3S)$, $He(2s^1S)$, $He(2p^3P)$, $He(2p^1P)$, $He(3s^3S)$, $He(3p^3P)$, He_2*, H*, H_2*,H_2(r), H_2(v), H_2O(v), $O(^1D)$, $O_2(^1\Delta)$, $O_2(^1\Sigma)$, O_2(r), O_2(v), O_3^*, OH(A)
Liquid Species	H_2O_{aq}, e_{aq}, $H_2O^+_{aq}$, $H_3O^+_{aq}$, H_2O_{2aq}, HO_{2aq}, OH_{aq}, OH^+_{aq}, OH^-_{aq}, H_{aq}, H_{2aq}, O_{aq}, O_{2aq}, $O_2^+{}_{aq}$, O_{3aq}, O^-_{aq}, $O_2^-{}_{aq}$, $O_3^-{}_{aq}$, $HO_2^-{}_{aq}$, He_{aq}, Ar_{aq}, Na^+_{aq}, Cl^-_{aq}, PFO^-_{aq}

Table 2 Radiation transport

Excited state	Energy (eV)	Wavelength (nm)
OH*	4.0	309 (broadband)
Ar_2*	9.9	126 (broadband)
$Ar(4s^1s_4)$	11.62	106.7
$Ar(4s^1s_2)$	11.83	104.8
Ar(4p)	12.91	96.0
$He(2^1P)$	21.22	58.4
He_2*	20.7	60 (broadband)
He(3P)	23.0	53.9

Reaction Mechanism

The species included in the gas- and liquid-phase reaction mechanism are listed in Table 1. In the gas phase, the mechanism consists of 20 charged species, 11 neutral ground-state species, and 26 neutral excited-state species. In the liquid, a total of 24 species are considered, where e_{aq} refers to solvated electrons. The gas-phase reaction mechanism is based on the work of Van Gaens and Bogaerts [40], with helium reactions incorporated following Norberg et al. [29] and Emmert et al. [41]. The liquid-phase reaction mechanism was adapted from Tian and Kushner [42], with additional reactions from Lietz and Kushner [43] and Meyer et al. [44]. Further reactions involving H_2O_{aq} were added and treated with the surfactant module, including dissociation, dissociative attachment, and ionization, based on gas-phase reaction data [10, 45].

Photoemission, photoionization, and photodissociation are included in the reaction mechanism. The photoemission tracked in this work are summarized in Table 2. In the gas phase, photons emitted from $Ar(4s^1s_4)$ [106.7 nm], $Ar(4s^1s_2)$ [104.8 nm], and Ar_2^* [126 nm] are absorbed by H_2O with a cross section of 10^{-17} cm^2, and from Ar(4p) [96 nm] with a cross section of 1.5×10^{-17} cm^2 [46]. Since the photon energies from the first three states lie below the ionization threshold of H_2O (12.6 eV), photoabsorption produces dissociation into OH and O. Due to the higher photon energy of Ar(4p) emission, photoabsorption leads to H_2O ionization. The ionization threshold of H_2O in the liquid phase is lower than in the gas phase, and photon energies above 7 eV can significantly ionize H_2O_{aq}. Following the experimental findings of Sander et al. [47], photons emitted by $Ar(4s^1s_4)$, $Ar(4s^1s_2)$, and Ar_2^* produce ionization of liquid water with a quantum yield of 0.6, with the remaining fraction contributing to dissociation. Radiation from all helium excited states ionize argon atoms in the gas phase with a cross section of 3.5×10^{-17} cm^2 [48, 49], and ionize H_2O molecules in

both phases with a cross section of 2.3×10^{-17} cm^2 [46]. Radiation from OH* [309 nm] can be reabsorbed by OH with a cross section of 1.4×10^{-16} cm^2 [50], whereas absorption by H_2O is negligible (cross section of the order of 10^{-24} cm^2) [51].

The surfactant PFO^-_{aq} can undergo dissociation through reactions with electrons, ions, radicals, and photons originating from the gas-phase plasma. Sapunaa et al. [52] recently computed the electron-impact dissociation cross sections of several PFAS, including PFOA, perfluorobutanoic acid (PFBA), perfluorobutanesulfonic acid (PFBS), and perfluorooctanesulfonic acid (PFOS). The dissociation pathways in [52] included excitation to singlet and triplet states, and dissociative ionization. In this work, due to the lack of specific data, we assume that the electron-impact dissociation cross sections for PFO^-_{aq} ($C_8F_{15}O_2^-{}_{aq}$) are the same as for $PFOA_{aq}$ ($C_8HF_{15}O_{2aq}$). The gas-phase rate coefficients for PFO^-_{aq} dissociation by argon and helium ions were taken from [53], being 2.4×10^{-9} cm^{-3} and 7.6×10^{-9} cm^{-3} for argon and helium ions, respectively. However, when applying Eq. (2) to calculate the effective cross section for the plasma-surfactant process, the resulting values exceed the surface-site area $A_s^{PFO} = 4.83 \times 10^{-15}$ cm^2 and are therefore limited to the physical area occupied by this molecule (cf. Sect. "Plasma-Surfactant Module"). PFO^-_{aq} dissociation by other ions (such as H_2O^+, H_3O^+ and OH^+) was neglected due to their lower ionization potentials. The gas-phase rate coefficients for PFO^-_{aq} dissociation by argon and helium excited states were estimated to be 4×10^{-11} cm^{-3}. This estimation is not critical as the flux of radicals to the surface of the liquid is much smaller than the flux of charged particles.

The VUV photon absorption cross section of PFO^- was measured in the gas phase by Douix et al. [54] for photon energies between 6 and 12 eV. In that work, two mechanisms of photoabsorption were identified: (i) photodissociation of PFO^- producing at least one ionic fragment, and (ii) photodetachment of PFO^-, which may also lead to dissociation, since $C_8F_{15}O_2$ is not a stable chemical state. However, only ion fragments could be detected, and so no definitive conclusions could be drawn regarding fragmentation following photodetachment [54]. Here, we assumed that photodetachment also contributes to dissociation. The impact of this assumption is discussed in Sect. "5". The cross section for photodissociation involving ion fragments has an onset near 7.6 eV and varies between 2.5×10^{-18} and 1×10^{-17} cm^2 for photon energies between 8 and 12 eV. The cross section for photodetachment has an onset near 6.4 eV and varies between 5×10^{-17} and 1.5×10^{-16} cm^2 for energies between 7 and 12 eV, being on average 30–40 times larger than for direct photodissociation. In this work, a total photodissociation cross section of PFO^-_{aq} of 10^{-16} cm^2 was assumed for all photons produced by argon and helium excited states (cf. Table 2). Note, however, that photodissociation has not been measured for photon energies higher than 12 eV, and so the value for helium radiation is an approximation.

The PFO^-_{aq} dissociation processes described above concern reactions driven by species originating directly from the plasma. However, PFO^-_{aq} can also undergo dissociation induced by solvated electrons. The rate coefficient for this process was measured by Maza et al. [55] to be approximately 2.3×10^{-12} cm^3 s^{-1} for PFO^-_{aq} concentrations below 1 mM (415 ppm).

Since the extent of PFO^-_{aq} dissociation during a single pulse is small compared to the total PFO^-_{aq} density, the subsequent chemistry of the decomposition products was not explicitly tracked. Accordingly, only the total PFO^-_{aq} dissociation is computed. We acknowledge that significant remediation of PFAS compounds requires many discharge pulses. Effective remediation of PFAS requires repeated pulsing and accounting for the fate of intermediate

products. That said, the focus of this work is to discuss how plasma operating conditions control the fluxes of reactive species incident on the liquid surface and to identify the initial reaction pathways governing PFAS dissociation.

APPJ Interaction with a Liquid Surface

The plasma properties of an APPJ interacting with a liquid surface were first examined in detail for the base case. This base case consists of a −15 kV pulse, an Ar/H_2O gas mixture of 99.5/0.5, and a liquid layer 2.4 mm thick with a conductivity of 0.1 mS/cm.

The electron density, *E/N* (electric field/gas density), and OH gas-phase density during a discharge pulse are shown in Fig. 2. The discharge is initiated by placing a neutral plasma seed at the tip of the electrode, with an initial density of 10^{11} cm^{-3} and a diameter of 500 µm. During the first 10 ns, a Townsend ionization wave propagates from the powered electrode towards the liquid surface. Upon reaching the liquid at 10 ns, the surface charges negatively, generating electric fields near the center of the liquid surface up to 72 kV/cm and *E/N* up to 290 Td (1 Td = 10^{-17} V-cm^2). The parallel components of the electric field initiate a surface ionization wave that propagates horizontally along the liquid surface. During this horizontal propagation, the electric field is largest at the streamer head, reaching *E/N* values of 250 Td and electron temperatures of 5 eV. Behind the streamer head, the electric field weakens due to charge shielding and the high conductivity of the plasma column, resulting in lower *E/N* values. Consequently, the majority of electron-impact generated reactivity occurs during the passage of the SIW head.

The electron density is confined within 500 µm above the surface, reaching up to 1.5×10^{16} cm^{-3} near the interface. The production of short-lived reactive species, such as OH, mostly mirrors the electron density profile. Far from the SIW where the electron den-

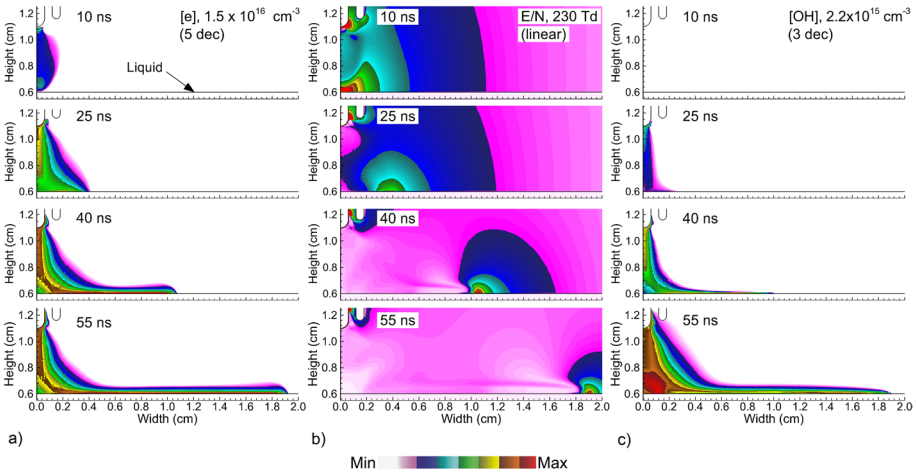

Fig. 2 Macroscopic plasma properties for the APPJ incident onto the liquid surface for the base case conditions. (**a**) Electron density with a 5-decade log scale, (**b**) reduced electric field, *E/N*, (1 Td = 10^{-17} V-cm^2) with a linear scale, and (**c**) OH gas-phase density with a 3-decade log scale. The maximum values are noted in the figures. Operating conditions are −15 kV, Ar/H_2O = 99.5/0.5, and liquid with 2.4 mm thickness and 0.1 mS/cm conductivity

sity is small, OH is produced by photodissociation of H_2O resulting from photoemission from excited argon states. The OH density reaches 2×10^{15} cm^{-3} after 55 ns.

From 10 to 55 ns, the SIW propagates 1.92 cm, corresponding to an average propagation speed of $\approx 4.3 \times 10^7$ cm/s. The SIW continues to propagate until the voltage pulse begins to decrease at 90 ns, after which it decelerates, ultimately reaching a maximum extent of 3.3 cm.

The fluences (time integral of flux which produces the number of incident particles per unit area) of photons, charged species, and electronically excited states onto the liquid surface are shown in Fig. 3 at the end of the discharge pulse (115 ns). The photon fluence is dominated by photoemission from the argon dimer, Ar_2*. Photoemission from atomic argon

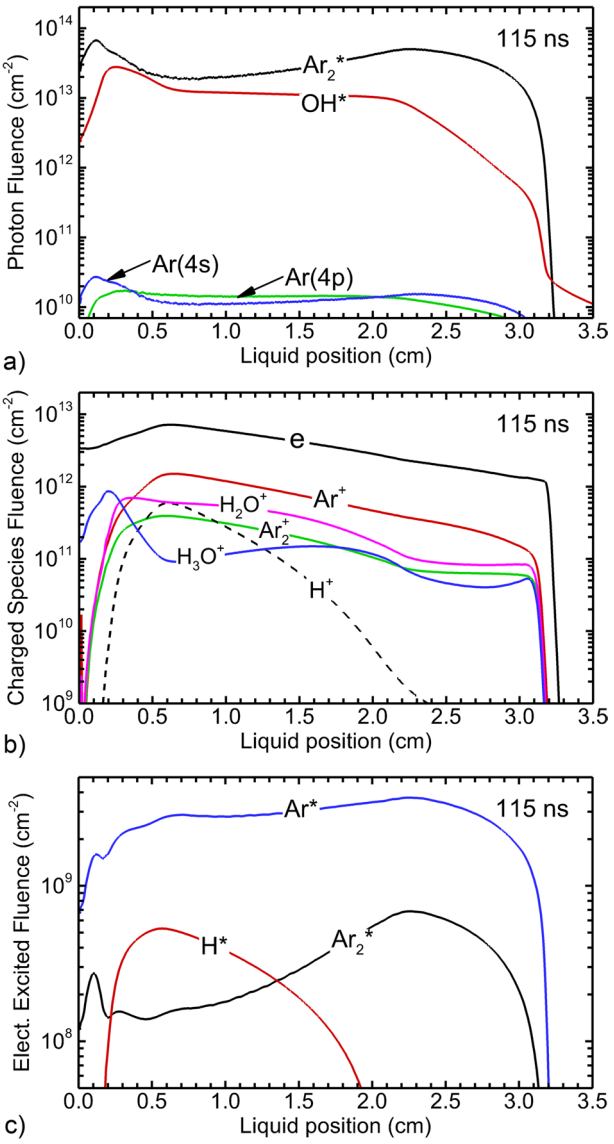

Fig. 3 Fluences (time-integrated flux) incident onto the liquid surface at 115 ns, for the base case. (**a**) Photon fluence, (**b**) electron and ion fluences, (**c**) electronically excited species fluences with energies above 10 eV. In (**a**), photoemission of Ar($4s^1s_4$) and Ar($4s^1s_2$) is combined into Ar(4s). In (**c**), all electronically excited states of atomic argon are combined into Ar*

– $Ar(4s^1s_4)$, $Ar(4s^1s_2)$, and Ar(4p) – is three orders of magnitude lower than that from Ar_2*. The Ar_2* excited state is efficiently produced at atmospheric pressure by the three-body reaction $Ar^* + Ar + Ar \rightarrow Ar_2^* + Ar$, where Ar* represents any excited state of atomic argon. The large disparity between dimer and atomic argon emissions primarily arises from differences in the effective emission coefficients. The natural emission coefficient of Ar_2* radiation is 6×10^7 s^{-1} [56], and this emission is not radiatively trapped. However, atomic resonant argon radiation is significantly trapped at atmospheric pressure, resulting in effective emission coefficients that are much smaller than their natural values [57]. Following the Holstein formalism, the effective emission coefficients for $Ar(4s^1s_4)$, $Ar(4s^1s_2)$, and Ar(4P) are 6×10^3 s^{-1}, 2.64×10^4 s^{-1}, and 2×10^4 s^{-1}[50]. As Ar* is depleted through dimer formation and atomic resonance radiation is heavily trapped, the fluence of Ar_2* excimer emission exceeds that of atomic argon resonance emission. Although the fluence of OH* radiation is significant, its photon energy (≈ 4 eV) is not sufficient to dissociate surfactant molecules, making it less relevant under the conditions considered in the present study.

The fluences of electrons and ions arriving at the liquid surface are shown in Fig. 3b. The dominant ion species reaching the surface is Ar^+, followed by H_2O^+, Ar_2^+, H_3O^+, and H^+ ions. Neither electron nor ion fluences peak at the center of the liquid. The initial Townsend avalanche negatively charges the liquid directly below the electrode, which produces lateral components of the electric field which divert the streamer that follows, as shown Fig. 2a. The electron fluence is approximately 8 times smaller than the Ar_2* photon fluence. Under these conditions, photons may have a significant influence on the plasma-liquid interfacial reactivity. However, the gas mixture plays a significant role in these trends, as discussed in Sect. "Gas Mixture: Argon/Helium Content".

The fluences of electronically excited species with energies above 10 eV arriving at the liquid surface are shown in Fig. 3c. Electronically excited states of atomic argon, here combined into Ar*, are the main energetic neutral species arriving at the liquid surface. However, their fluence is approximately three orders of magnitude lower than that of charged species. As a result, in spite of the high intrinsic reactivity of electronically excited species with surface resident species, their lower fluence onto the surface reduces their role in producing plasma-liquid reactivity compared to photons and charged species.

Controlling Plasma-Liquid Interfacial Reactivity

In this section, the plasma-liquid interfacial reactivity is analyzed as a function of applied electrode voltage, liquid conductivity, liquid thickness, and gas mixture. The effect of applied voltage is discussed more briefly since it was previously addressed in [10]. The influence of these conditions on the propagation of the SIW is discussed, and the resulting variations in fluences of electron and photons onto the liquid surface are quantified. Only VUV photon radiation is included in this analysis – specifically, radiation from argon and helium excited states – while OH* emission (4 eV) is excluded due to its low energy and inability to initiate the in-liquid chemistry of interest. To facilitate comparison, the parametric studies are performed by varying one parameter at a time relative to the base case described in the preceding section (−15 kV pulse, $Ar/H_2O = 99.5/0.5$ gas mixture, 2.4 mm liquid thickness, and 0.1 mS/cm liquid conductivity).

Powered Electrode Voltage

The propagation of the SIW can be interpreted as a continuous charging of the underlying liquid capacitance. The extent of propagation is therefore largely determined by the rate of charging of this capacitance, which in turn depends on the charged particle fluence to the surface delivered by the gas phase plasma. Higher applied electrode voltages are expected to generate a stronger volume ionization wave, enabling faster charging of the liquid capacitance and propagation across a larger extent of the liquid surface.

VUV photon and electron fluences onto the liquid surface are shown in Fig. 4 at the end of the pulse (115 ns) for voltages between −12 and −17 kV. For −12 kV, the plasma fluences are negligible beyond 1.8 cm due to the slowly propagating SIW, whereas for −17 kV the

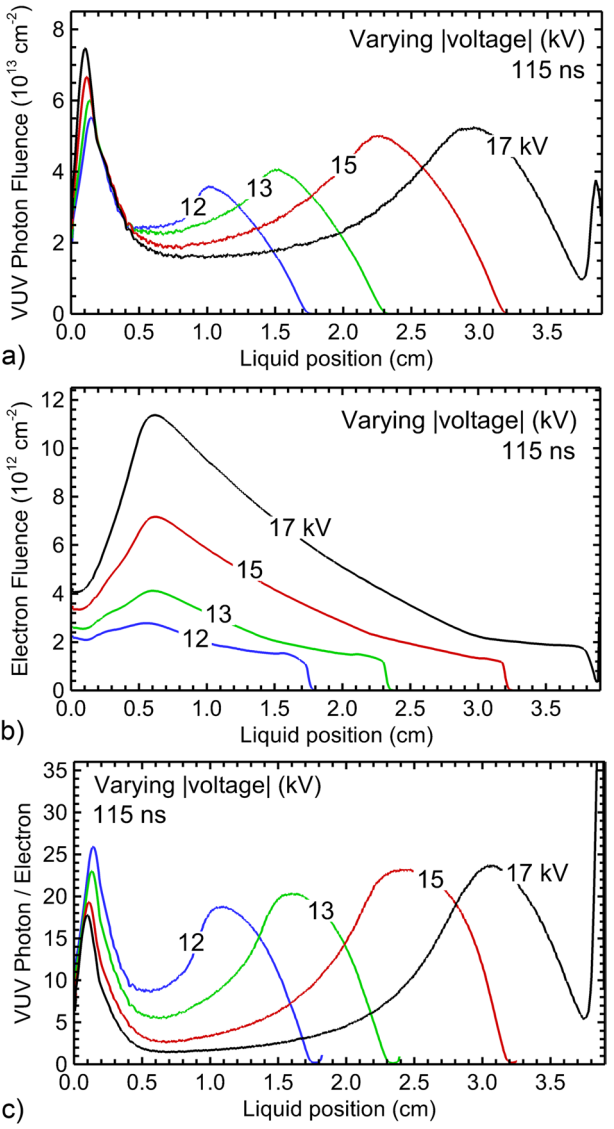

Fig. 4 Fluences (time-integrated flux) across the liquid surface at 115 ns, for different applied voltages. (**a**) VUV photon fluence, (**b**) electron fluences, (**c**) ratio of VUV photon to electron fluences. Other operating conditions are the same as the base case

SIW propagates to the outer boundary of the reactor at 3.9 cm. In addition to the extent of propagation, both the magnitude and spatial profile of the fluences vary significantly with voltage. The photon fluence has two maxima – near the center of the reactor and at the maximum extent of the SIW. With increasing voltage magnitude, the maximum VUV photon fluence near the axis increases from 5.5×10^{13} cm^{-2} to 7.5×10^{13} cm^{-2} with contributions from the initial Townsend discharge. The maximum in fluence at the outer extent of the SIW increases from 3.6×10^{13} cm^{-2} to 5.2×10^{13} cm^{-2}. The change in the spatial profile of the VUV fluence can be attributed to two factors. The first is the faster propagation of the SIW at higher voltages, which results in a shorter residence time of the streamer head at intermediate liquid positions and, consequently, fewer argon excited states generated at those locations. The second factor is related to the higher *E/N* of the SIW head in intermediate positions for higher voltages. Since the ratio of excitation collisions to ionization collisions decreases with increasing *E/N*, for higher voltages and intermediate positions, the importance of excitation collisions decreases, thereby affecting VUV emission.

In contrast to the VUV fluence, the electron fluence increases sharply with voltage magnitude. From −12 to −17 kV, the peak electron fluence rises from 2.8×10^{12} cm^{-2} to 11.4×10^{12} cm^{-2}. As a result, the ratio of VUV photon fluence to electron fluence can be controlled by adjusting the electrode voltage, shifting from more photon-dominated fluxes delivered to the surface to a more electron-dominated regime as voltage increases (see Fig. 4c). Such control is limited by the minimum voltage required for initiating SIW propagation, below which the charging of the liquid surface is insufficient to sustain the SIW. However, even at the highest voltage investigated here, the photon fluence remains larger than the electron fluence.

Liquid Conductivity

Although the liquid conductivity cannot be readily controlled for many plasma-liquid applications, this property can significantly impact the propagation of the SIW, as it governs the dielectric losses in and conduction current through the liquid. As conductivity increases, a larger fraction of the discharge current is diverted through the liquid towards the ground electrode, rather than sustaining horizontal current flow along the interface. This redistribution of current reduces the electric field available to support SIW propagation, leading to a decrease in the maximum spatial extent of the SIW with increasing liquid conductivity.

The spatial profiles of the electron density and reduced electric field (*E/N*) are shown in Fig. 5 for liquid conductivities between 0 and 1 mS cm^{-1}. The times for each image were selected to capture the head of the SIW at comparable positions across all conductivities. Taking into account that the initial plasma streamer reaches the liquid surface approximately 10 ns after the beginning of the voltage pulse, the SIW requires 39.5 ns to arrive at 1.76 cm for a liquid with zero conductivity, corresponding to an average propagation speed of 4.5×10^7 cm s^{-1}. For a conductivity of 1 mS cm^{-1}, the SIW takes 67 ns to reach the same position, corresponding to an average speed of 2.6×10^7 cm s^{-1}, 40% smaller than in the absence of conductivity. These trends of decreasing propagation speed with increasing conductivity are in agreement with the experimental observations of Hermann et al. [24, 25]. While for lower conductivities the electron density profile is detached near the center of the liquid, at the highest conductivity the profile becomes continuous and strongly focused at the center.

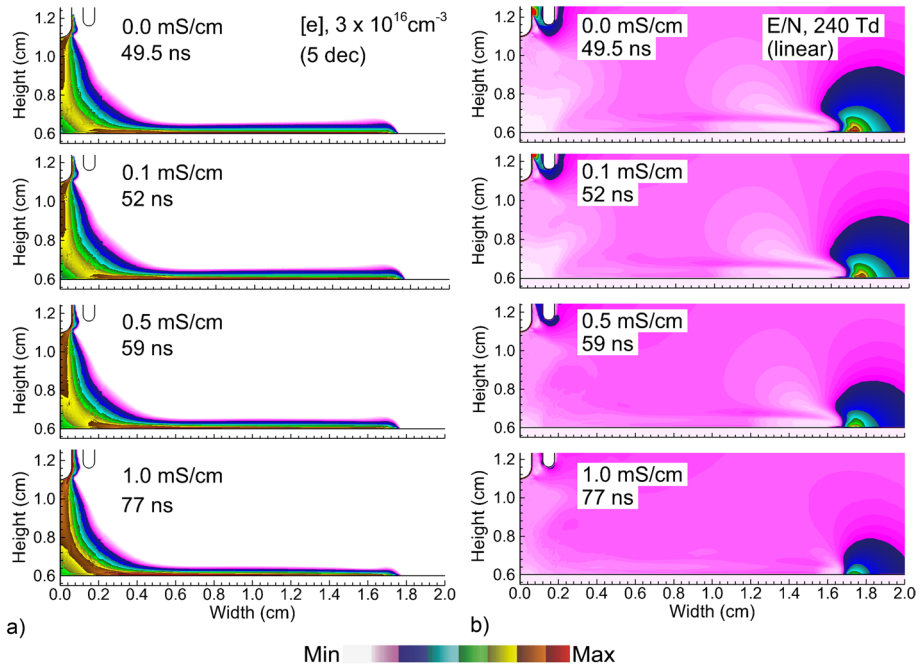

Fig. 5 Macroscopic plasma properties for the APPJ incident onto the liquid surface for different liquid conductivities. (**a**) Electron density with a 5-decade log scale and (**b**) reduced electric field, *E/N*, with a linear scale. The maximum values are noted in the figure. The times for each image were chosen to capture the SIW at near the same position. Other operating conditions are common to the base case.

Liquid conductivity affects the net charge density at the surface of the liquid, which in turn influences the electric field. As shown in Fig. 5b, the *E/N* at the SIW head decreases significantly with increasing conductivity, ranging from 258 Td at 0 mS cm^{-1} to 130 Td at 1 mS cm^{-1} at the position shown in the figure. Consequently, the reactivity per electron at the SIW head is expected to be higher for lower conductivities.

VUV photon and electron fluences onto the liquid surface are shown in Fig. 6 at the end of the discharge pulse (115 ns) for different liquid conductivities. For 0 mS cm^{-1}, the plasma fluences cover the entire liquid surface (up to 3.9 cm), whereas for the highest conductivity of 2 mS cm^{-1}, the fluences do not exceed 1.8 cm. This behavior is associated with the lower electric field at the SIW for higher conductivities, which limits the propagation distance. In addition to the reduced propagation extent, the spatial profile of the electron fluence is strongly affected by conductivity, becoming increasingly focused at the center for higher conductivities. As the conductivity rises from 0 to 2 mS cm^{-1}, the peak electron fluence increases from 5.9×10^{12} to 3.7×10^{13} cm^{-2}.

The divergence of the initial streamer and SIW from the center of the reactor results from negatively charging the surface of the liquid during the Townsend discharge stage. At low conductivity, the surface charge is retained (dielectric relaxation time exceeds the discharge duration). The surface charge diverts the subsequent streamer and SIW from the center of the reactor. With increasing conductivity, the surface charge is dissipated into the bulk liquid as current (dielectric relaxation time decreases) which then reduces or eliminates the diver-

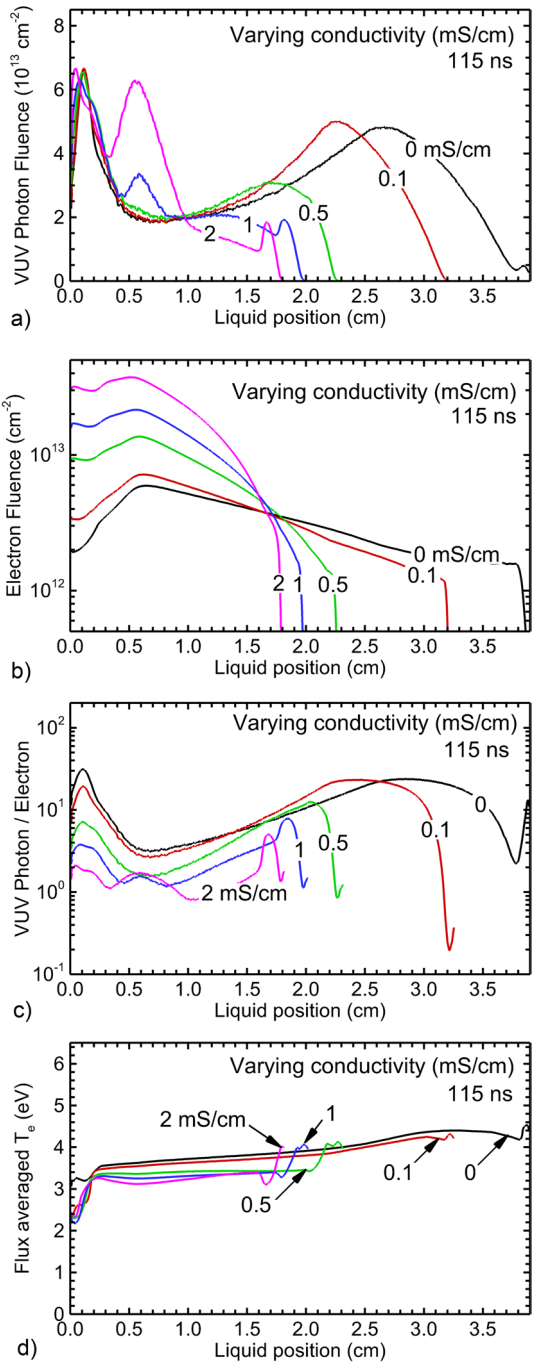

Fig. 6 Fluences (time-integrated flux) across the liquid surface at 115 ns, for different liquid conductivities. (**a**) VUV photon fluence, (**b**) electron fluences, (**c**) VUV photon to electron fluences, (**d**) Flux-averaged electron temperature. Other operating conditions are the same as the base case

sion of the subsequent streamer and SIW. The decrease in spatial extent of the SIW with increasing conductivity is partly explained by current continuity being accomplished by conduction current flowing through the liquid. For low conductivities, current continuity is maintained by displacement current through the liquid, which requires successive charging of the surface of the liquid by a propagating SIW.

In contrast, the VUV photon fluence decreases with increasing liquid conductivity. VUV photon fluxes are produced in the gas phase by electronic excitation which dominantly occurs at the head of the SIW. With increasing conductivity, the E/N in the head of the SIW decreases which in turn decreases the rate of excitation of electronic states, thereby reducing VUV fluences. As a result, the ratio of VUV photon to electron fluence onto the liquid, shown in Fig. 6c, decreases with increasing conductivity. With increasing conductivity, there is a transition from fluences being photon-dominated to fluences being more electron-dominated. Although more electrons reach the liquid surface at higher conductivities, their flux-averaged temperature decreases moderately with conductivity, as shown in Fig. 6d.

Liquid Layer Thickness

The electrical capacitance of the liquid layer is $\varepsilon_0 \varepsilon_r A/d$, where ε_0 is the vacuum permittivity, ε_r is the relative permittivity of the liquid ($\varepsilon_r \approx 80$ for water), and A and d are the area and thickness of the layer. Thinner layers therefore have higher capacitances, which can sustain larger surface charge densities and generate stronger SIWs. Since the liquid thickness can be readily adjusted in experimental reactors, this parameter serves as a practical means of controlling interfacial reactivity.

The electron density and *E/N* profiles of the SIW are shown in Fig. 7 for liquid thicknesses between 0.8 and 5 mm. The time for each image was chosen to capture the SIW head at similar positions. The higher capacitance of thinner liquid layers leads to larger electron densities both near the surface and in the bulk plasma. From a thickness of 0.8 to 5 mm, the maximum electron density near the surface decreases from 5×10^{16} to 7×10^{15} cm^{-3}. The larger electron density with thinner layers is associated with a higher net charge density at the head of the wave, which in turn produces a larger electric field. Consequently, as the thickness increases from 0.8 to 5 mm (smaller capacitance), the *E/N* at the SIW head decreases from 275 to 185 Td. Similar to the change in *E/N* when changing conductivity, this reduction in *E*/N can significantly influence the interfacial reactivity.

The SIW propagation speed depends on the liquid thickness. For a liquid thickness of 0.8 mm (large capacitance), the SIW reaches 1.76 cm in 34 ns (speed of 5.2×10^7 cm s^{-1}), whereas for 5 mm (small capacitance), the SIW requires 56 ns to reach the same distance (speed of 3.1×10^7 cm s^{-1}), corresponding to a decrease of 39% in speed. This result reflects the coupling between the local surface capacitance, surface charge accumulation, and charge production in the head of the SIW. If the rate of charge production is constant, the larger capacitance of thinner liquids would require more charge to reach a given surface potential, which would tend to increase the charging time. However, for these conditions the rate of charge production is not constant. Thinner liquid layers are more strongly capacitively coupled to the grounded electrode, enabling larger charge densities to be sustained in the head of the SIW. The resulting increase in *E/N* enhances ionization and charge production, thereby decreasing the charging time and increasing the SIW propagation speed. This

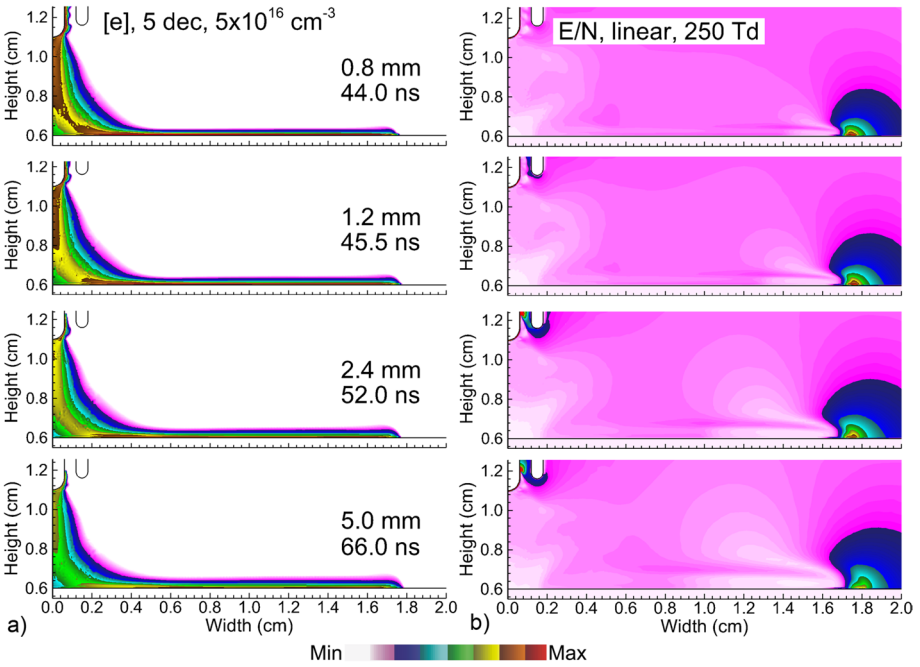

Fig. 7 Macroscopic plasma properties for the APPJ incident onto the liquid surface, for different liquid thicknesses. (**a**) Electron density with a 5-decade log scale, (**b**) reduced electric field, *E/N*, with a linear scale. The maximum values of each scale are noted in the figure. The times for each image were chosen to capture the SIW at near the same position. Other operating conditions are the same as the base case

enhanced charge production dominates over the slower charging expected from the larger capacitance alone.

Under different configurations of the reactor, the SIW speed may scale differently with thinner liquids having higher capacitance exhibiting slower propagation. In the current configuration, the ground electrode is in direct contact with the liquid, such that the series capacitance between the SIW and ground is determined solely by the liquid layer. In contrast, when the liquid is contained in a glass or plastic dish with the ground electrode positioned beneath the dish, the effective series capacitance includes contributions from both the liquid and the dielectric dish.

The VUV photon and electron fluences at the end of the pulse are shown in Fig. 8 for different liquid thicknesses. For a thickness of 5 mm, plasma fluences do not extend beyond 2.7 cm, whereas for 0.8 mm, the maximum extent is 3.4 cm. The reduced extent for thicker layers results from the lower *E/N* at the SIW head.

While the magnitude of VUV fluences remains similar across the different thicknesses, the spatial profile changes significantly. For thinner layers, the photon fluence is higher at the edges than in the middle, whereas for thicker layers, the fluence is more uniform along the liquid surface. This behavior is analogous to that observed for voltage variation. Edge-peaked VUV fluences are associated with both faster SIW propagation and the decrease of electron-impact excitation compared with electron-impact ionization at intermediate positions, which in turn is caused by a higher *E/N* in those regions.

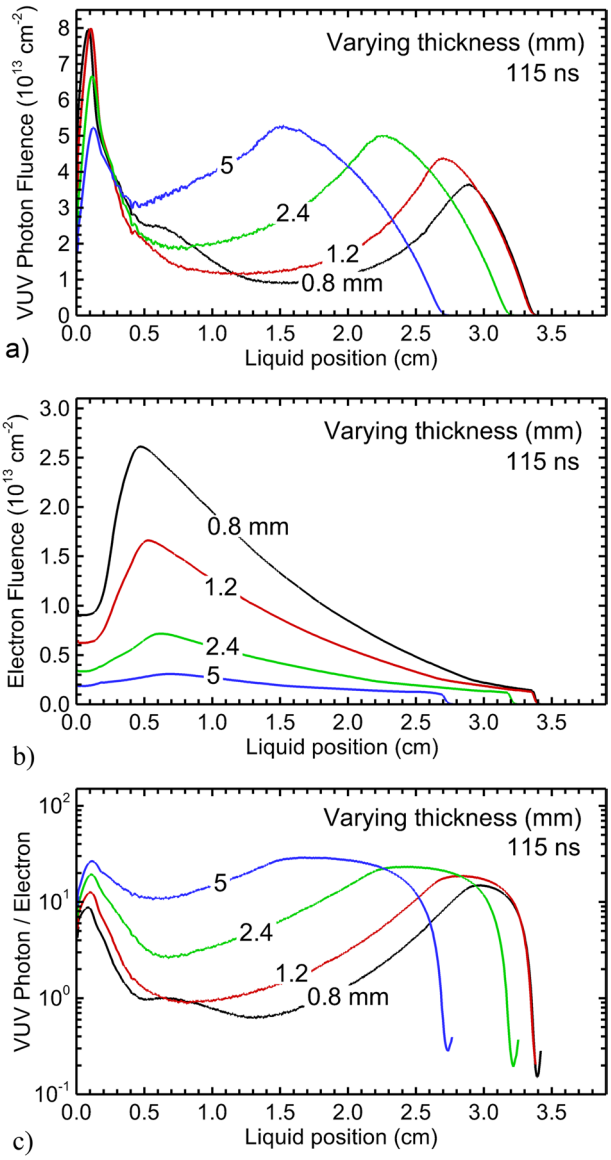

Fig. 8 Fluences (time-integrated flux) across the liquid surface at 115 ns, for different liquid thicknesses. (**a**) VUV photon fluence, (**b**) electron fluences, (**c**) VUV photon to electron fluences. Other operating conditions are the same as the base case.

The electron fluence is strongly influenced by the thickness of the liquid layer. From 0.8 to 5 mm, the peak electron fluence decreases from 2.6×10^{13} cm^{-2} (high capacitance) to 3.0×10^{12} cm^{-2} (low capacitance) corresponding to a 89% reduction. This result suggests that liquid thickness is a promising parameter for tuning interfacial reactivity, enabling transitions from photon-dominated to electron-dominated regimes. This trend is quantified by the corresponding VUV photon-to-electron fluence ratio shown in Fig. 8c.

Gas Mixture: Argon/Helium Content

Up to this point, the initial background gas mixture was the same as the base case (Ar/H_2O=99.5/0.5). The choice of gas species determines the characteristics of the bulk plasma, the rate of surface charging, and the production of reactive species that ultimately reach the liquid surface. In this section, the impact of gas composition is examined by varying the argon/helium atomic ratio, from 1/0 to 0/1, while maintaining a constant 0.5% H_2O.

For argon, the first inelastic process has an energy threshold of 11.5 eV and the ionization threshold is 16 eV. For helium the first inelastic threshold occurs at 19.8 eV and the ionization threshold is 24.6 eV. This wide difference in the spectrum of electron energy losses can lead to considerably different SIW dynamics. For instance, for E/N=200 Td and Ar/H_2O=99.5/0.5, only 21% of the electron power is dissipated in ionizing collisions, with the majority of the rest of the power being dissipated in electronic excitation. For the same E/N and He/H_2O=99.5/0.5, the electron power losses are equally shared between ionization and electronic excitation.

The spatial profiles of the electron density and average electron temperature (T_e) are shown in Fig. 9 for various helium fractions. As the helium fraction increases, the electron density profile becomes significantly thicker above the water surface. This behavior arises from two main factors. On the one hand, the higher inelastic thresholds of helium increase the average electron temperature and promote additional ionization in the outer regions of the main discharge channel. Although electrons in the outer regions may not be energetic enough to ionize He (24.6 eV), they are sufficiently energetic to ionize H_2O (12.6 eV) and Ar (15.8 eV). On the other hand, VUV emission from any helium excited state can ionize both H_2O and Ar, while in argon only Ar(4p) emission contributes to H_2O ionization in the gas phase, further explaining the broadening of the electron density profile in helium-containing mixtures.

The SIW propagation speed increases with helium fraction. The average propagation speed, calculated from the moment the initial streamer reaches the liquid surface until the head of the SIW arrives at 1.76 cm, is 4.2×10^7, 5.4×10^7, 7.5×10^7, 1.1×10^8, and 1.3×10^8 cm/s, for helium percentage fractions of 0, 25, 50, 75, and 100, respectively. This increase in speed is not associated with a higher electric field, as the E/N at the head is not increasing with helium content. The E/N in the head of the SIW is 241, 238, 233, 234, and 220 Td, for the same sequence of increasing He content. Instead, the faster propagation is attributed to the higher electron mobility in helium-rich mixtures. For instance, at E/N=200 Td, the electron mobility in pure helium is 3.2 times larger than in pure argon.

The average electron temperature of the SIW (shown in Fig. 9b) increases with helium fraction, reflecting the higher energy thresholds of helium. The peak T_e at the SIW head ranges from 4.9 to 9.2 eV with increasing He content, with a steeper temperature rise occurring for higher helium content.

The VUV photon and electron fluences at the end of the voltage pulse are shown in Fig. 10 for different helium fractions. For finite argon fractions, the VUV photon fluence scales nearly linearly with the argon content. In contrast, for pure helium, the VUV fluence is approximately two orders of magnitude lower than for pure argon. Argon VUV radiation dominates over helium radiation due to the lower threshold of the Ar resonant states (11.5 eV for Ar compared to 21 eV for He) and the larger absorption probability of He produced radiation in the gas phase. Consequently, varying the argon/helium ratio in the gas

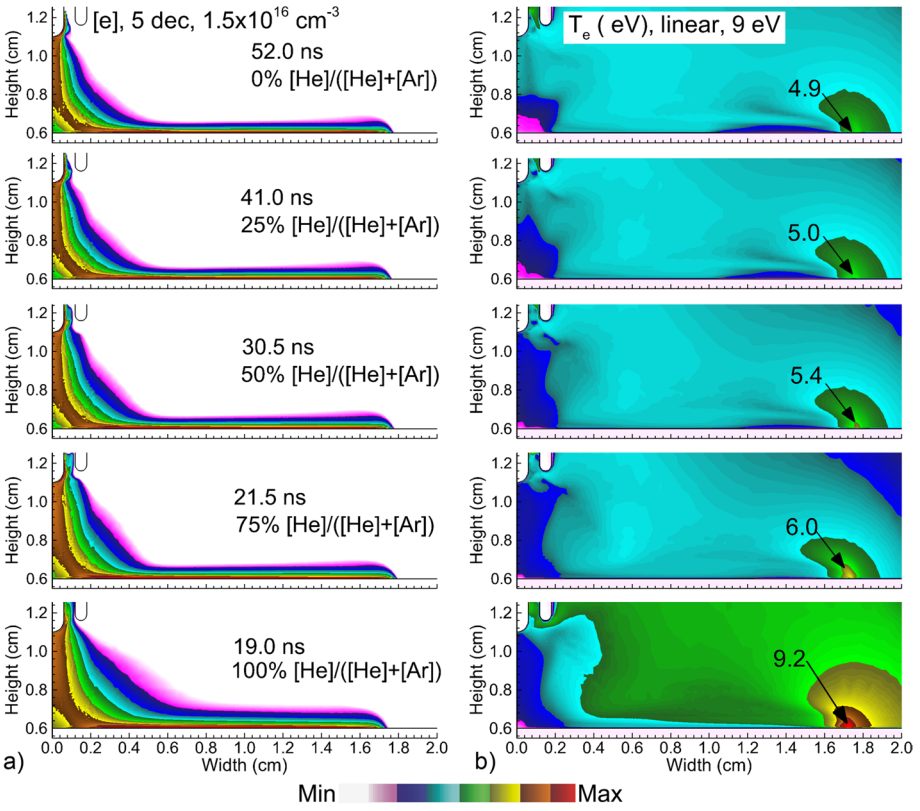

Fig. 9 Macroscopic plasma properties for the APPJ incident onto the liquid surface, for different argon/helium ratios. (**a**) Electron density with a 5-decade log scale, (**b**) electron temperature, T_e. The maximum values for each image are noted in the figure. The times for each image were chosen to capture the SIW at near the same position. Other operating conditions are the same as the base case

mixture provides an effective means of controlling the VUV fluences. Although the higher-energy radiation from helium states can initiate additional reaction pathways compared to argon, the VUV fluence in argon is two orders of magnitude higher, which is expected to more than compensate for this effect.

The peak electron fluence increases monotonically with helium content, ranging from 7.2×10^{12} to 1.6×10^{13} cm^{-2} for helium fractions between 0 to 100%, as shown in Fig. 10. This behavior is associated with the larger fraction of electron power being spent in ionizing collisions, as the helium fraction increases. The VUV-photon-to-electron fluence ratio strongly depends on the helium fraction in the gas mixture. In particular, for 100% He, the ratio of VUV-photon-to-electron fluence is much less than unity, indicating that under these conditions charged particles dominate the plasma-liquid reactivity.

Inventory of Plasma Particles onto the Liquid

This section summarizes the variations in interfacial reactivity discussed in Sects. "Powered Electrode Voltage" – "Liquid Conductivity", by means of the total inventory of particles

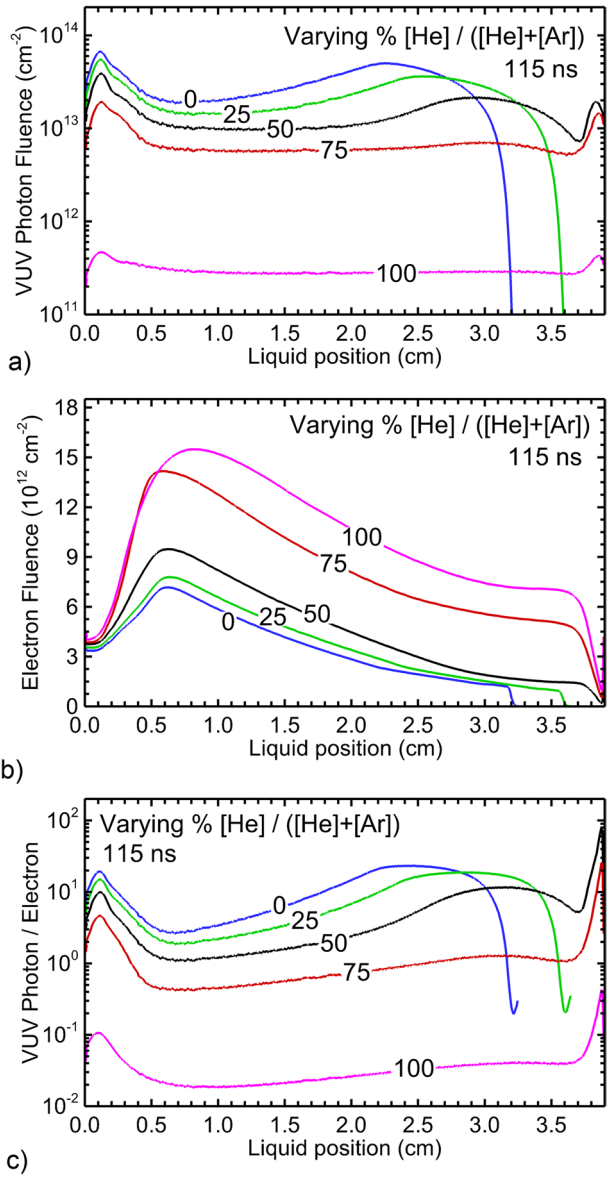

Fig. 10 Fluences (time-integrated flux) across the liquid surface at 115 ns, for various helium fractions. (**a**) VUV photon fluence, (**b**) electron fluences, (**c**) VUV photon to electron fluences. Other operating conditions are the same as the base case

incident on the liquid surface. The total inventory is defined as the total number of particles arriving at the liquid surface. The inventory is then the time- and surface-integrated flux of an incoming species. The total inventories of VUV photons and electrons impinging on the liquid surface are shown in Fig. 11, as a function of a) applied voltage, b) liquid conductivity, c) liquid thickness, and d) helium fraction in the gas mixture. Solid lines (left axis) represent the total inventory. Dashed lines (right axis) correspond to the total inventory normalized by the discharge energy, defined here as inventory efficiency, which is more relevant from a practical perspective.

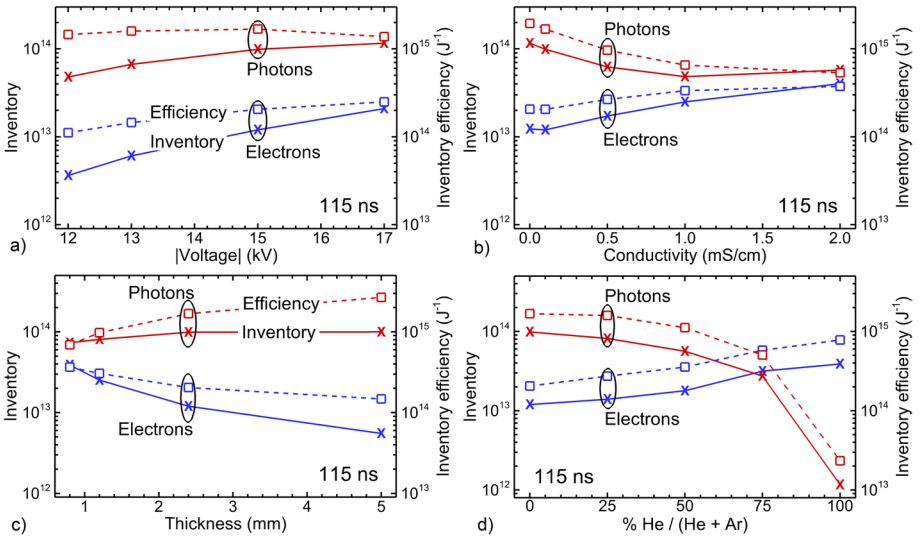

Fig. 11 Total inventories of VUV photons and electrons onto the liquid surface, as a function of: (**a**) magnitude of applied voltage, (**b**) liquid conductivity, (**c**) liquid thickness, and (**d**) helium fraction in gas mixture. Full lines and left axis represent the total inventory. Dashed lines and right axis represent the inventory efficiency (inventory divided by discharge energy)

The incident inventories of both VUV photons and electrons increase with applied voltage. However, the efficiency of photon production remains approximately constant, whereas the efficiency of electron production increases. This behavior reflects the rise in electron temperature near the plasma-liquid interface at higher voltages, which shifts a larger fraction of the deposited energy into ionizing collisions. In contrast, VUV photon production is governed largely by lower-threshold excitation processes. Electron fluxes contributing to the inventory originate within several mean-free-paths of surface whereas VUV photon inventories have contributions from emission originating from regions remote from the interface. As a result, VUV photon inventories are less sensitive to local electron heating. Increasing liquid conductivity suppresses the VUV photon inventory while enhancing electron delivery to the interface. In this regime, the trends for inventory efficiency follow those for absolute inventories. The dependence of electron and VUV photon inventories on liquid thickness have the opposite dependence. Thicker liquids favor VUV photon inventories but decrease electron inventories. Finally, increasing the helium content sharply reduces the photon inventory while increasing the electron inventory.

The optimal experimental configuration and operating conditions depend on the intended application. If the relevant reactions in the liquid are primarily driven by VUV photons, the most favorable conditions correspond to low-conductivity, thicker liquids, and argon-rich gas mixtures. In contrast, if the dominant reactions are initiated by incident electrons, the opposite conditions—higher conductivity, thinner liquids, and helium-rich mixtures—are more suitable.

Impact on Surfactant Perfluorooctanoate Dissociation

To evaluate the impact of plasma-liquid interactions on PFAS degradation, simulations were performed using a liquid bulk concentration of 1 ppm perfluorooctanoate anion. The total PFO^-_{aq} dissociation per unit liquid surface area, as a function of lateral position, is shown in Fig. 12 for gas mixtures of (a) Ar + 0.5% H_2O and (b) He + 0.5% H_2O. The total dissociation is separated into contributions from different incident species: gas-phase electrons (e), gas-phase ions (M^+), VUV photons (hν), and solvated electrons (e_{aq}). For the argon-based mixture, the two dominant dissociation pathways are initiated by incident gas-phase ions and VUV photons, followed in decreasing importance by solvated electrons and incident gas-phase electrons. For the helium-based mixture, the dissociation is dominated by gas-phase ions, while photon-induced dissociation is significantly reduced. The importance of incident gas-phase electrons increases compared to solvated electrons due to the higher electron temperature of the SIW in helium-based mixtures.

Although for argon mixtures VUV photon fluence dominates over charged-particle fluence for all of our conditions (Fig. 11), dissociation by incident gas-phase ions is larger than by VUV photon dissociation. The cause of this behavior is that the surfactant dissociation rate is proportional to both the incident species flux and the reaction cross section (Eq. 1). Under these conditions, the dissociation cross section by incident ions (limited to the PFO^-_{aq} site area) is much larger than the VUV photon cross section.

The red dashed line in Fig. 12a represents the dissociation of PFO^-_{aq} when VUV photodissociation resulting from electron detachment is neglected. In this regard, the absorption

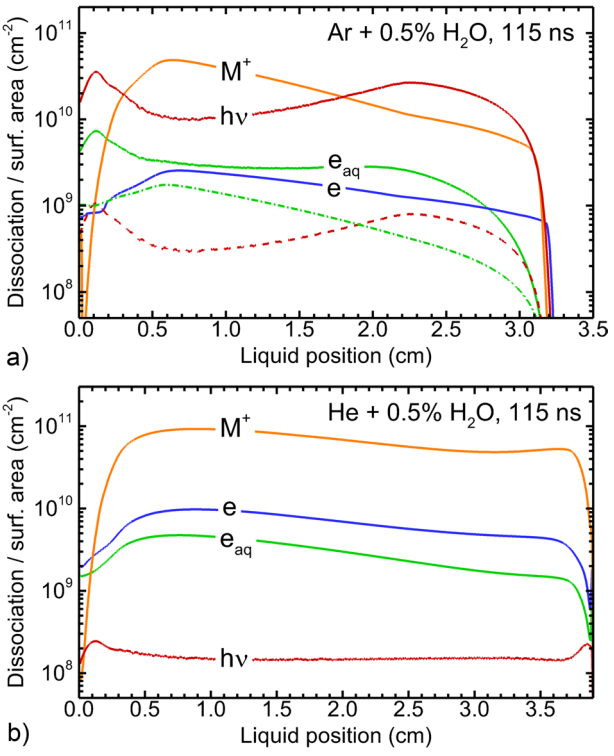

Fig. 12 PFO^-_{aq} dissociation per liquid surface area along the lateral position, after 115 ns, for (**a**) argon and (**b**) helium discharges. PFO^-_{aq} dissociation by different species are shown: gas-phase electrons (**e**), gas-phase ions (M^+), VUV photons (hν), and solvated electrons (e_{aq}). The red dashed curve represents VUV photon dissociation when the photodetachment contribution is neglected. The green dot-dashed curve represents dissociation by solvated electrons when photoionization in the liquid is neglected

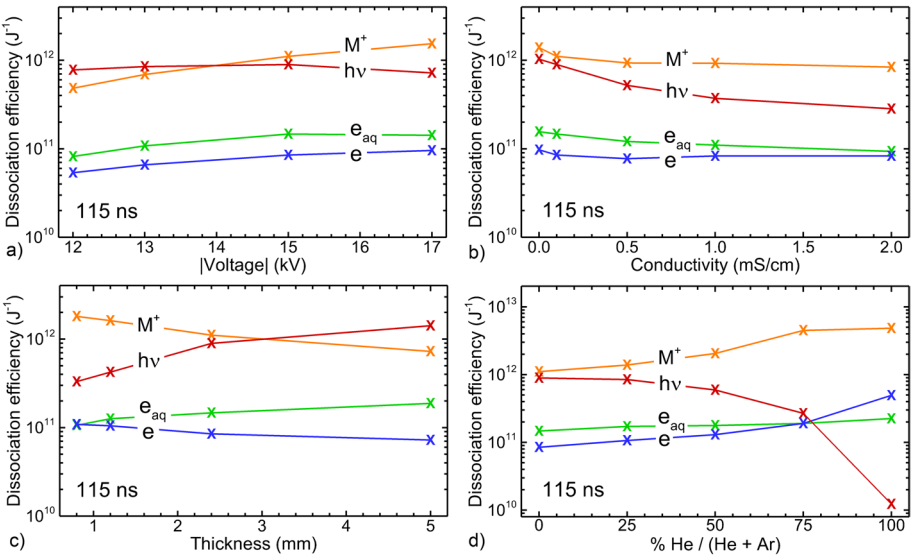

Fig. 13 PFO^-_{aq} dissociation efficiency as a function of: (**a**) magnitude of applied voltage, (**b**) liquid conductivity, (**c**) liquid thickness, and (**d**) helium fraction in gas mixture. Dissociation is separated into contributions from different species: gas-phase electrons (**e**), gas-phase ions (M^+), VUV photons (hν), and solvated electrons (e_{aq}).

cross section is 3×10^{-18} cm^2 instead of 10^{-16} cm^2. When neglecting dissociation following photo-detachment, VUV-induced dissociation makes a smaller contribution and is no longer comparable to dissociation produced by gas-phase ions. However, as discussed in Sect. "Operating Conditions", the contribution of photodetachment does likely contribute to photodissociation, since the product of PFO^-_{aq} photodetachment is not a stable chemical state and likely undergoes subsequent fragmentation.

The green dot-dashed line in Fig. 12 corresponds to the PFO^-_{aq} dissociation by solvated electrons if photoionization in the liquid is neglected. This contribution is approximately 3 times smaller than in the base case, highlighting that for these conditions photoionization in the liquid is the primary mechanism for producing solvated electrons in argon gas mixtures. In contrast, for the helium gas mixture shown in Fig. 12b, PFO^-_{aq} dissociation by solvated electrons is not affected by neglecting liquid-phase photoionization. This result is due to the smaller photon flux incident onto the liquid in helium compared to argon, such that solvated electrons are predominantly generated by the incident electron flux from the gas phase.

As discussed in the previous section, the incident fluences of plasma species vary significantly with operating conditions. Consequently, the relative importance of each species for PFO^-_{aq} dissociation also changes. The PFO^-_{aq} dissociation efficiency is shown in Fig. 13 as a function of: a) magnitude of applied voltage, b) liquid conductivity, c) liquid thickness, and d) helium fraction in the gas mixture. Here, the dissociation efficiency is defined as the total number of dissociated PFO^-_{aq} molecules normalized by the discharge energy.

The dissociation efficiency associated with charged species increases with applied voltage, whereas the photon efficiency slightly decreases at the highest voltage. Increasing liquid conductivity slightly decreases the efficiency of incident charged species and solvated electrons, and substantially suppresses photon-induced dissociation. Photon effi-

ciency is higher for thicker liquid layers, whereas dissociation by gas-phase charged species decreases. Finally, as the helium fraction in the gas mixtures increases, the contribution from charged species increases, while photon efficiency decreases. Although incident electron fluence increases with helium content, dissociation efficiency by solvated electrons increases only marginally, reflecting the concurrent reduction in VUV photon flux that limits photoionization in the liquid phase.

Concluding Remarks

Pulsed atmospheric plasmas incident on liquid layers were computationally investigated using a 2D hydrodynamics model. The primary objective of this work was to investigate methods to control the properties of the surface ionization wave (SIW) formed once the bulk plasma reaches the liquid surface, thereby controlling the reactive fluxes to the liquid. Several parameters of the plasma-liquid system were examined, including: the voltage pulse amplitude, liquid thickness, liquid conductivity, and the argon/helium gas mixture ratio, with a constant 0.5% water vapor.

The study focused on configurations relevant to PFAS remediation in water, for which the SIW properties are critical due to the surfactant behavior of some long-chain PFAS at the interface. The impact on plasma-liquid reactivity was quantified through the resulting electron and VUV-photon fluences onto the liquid surface, as well as the dissociation of the perfluorooctanoate anion, contained in the liquid phase and concentrated at the surface.

Higher voltage magnitude generates a stronger volume plasma, enabling faster charging of the liquid surface and propagation of the SIW across a substantially larger portion of the interface. As a result, the inventory efficiency of electrons onto the liquid surface significantly increases with voltage, whereas the photon efficiency remains approximately constant.

Liquid conductivity provides an alternative through-liquid pathway for discharge conduction current to reach ground and maintain current continuity, reducing the need to sustain a horizontally propagating SIW to maintain current continuity through displacement current. Consequently, as conductivity increases, the electron density profile becomes more focused near the center of the liquid, and the inventory efficiency of electrons is larger than that of photons.

As the thickness of the liquid layer is inversely proportional to its electrical capacitance, thinner liquids allow for greater surface charging, which enhances the formation of stronger SIWs and increases the efficiency of electron delivery to the surface. In contrast, VUV photon inventory onto the surface is more efficient for thicker liquids.

The effect of the gas mixture was examined by varying the argon/helium content from 1/0 to 0/1. SIWs in helium-containing mixtures propagate faster, owing to the larger electron mobility in helium compared with argon, which is itself a consequence of differences in the spectra of electron energy losses. Electron inventory efficiency increases with helium content, whereas photon inventory efficiency decreases sharply—by two orders of magnitude from 0 to 100% helium content. Fewer VUV photons are delivered to the liquid surface in pure helium than in argon, in part due to the higher threshold energies in He for electronic excitation, larger rates of quenching of excited states by water vapor and more absorption of He-produced radiation by water vapor.

The dissociation of the surfactant PFO^-_{aq} was investigated for these operating conditions. In general, surface dissociation of PFO^-_{aq} by incident ions originating from the plasma was the dominant pathway. In pure argon, surfactant dissociation by incident VUV photons was significant and of the same order as dissociation by ions. For most conditions, PFO^-_{aq} dissociation by solvated electrons in the liquid bulk was found to be comparable to dissociation by direct electron impact from the plasma, but less relevant than dissociation by incident ions. In argon gas mixtures, solvated electrons are dominantly generated through photoionization in the liquid phase, while in pure helium, they are mostly generated through the direct solvation of the incident electron flux. Radiation from the argon dimer (Ar_2*) can be a dominant source of electron production in the liquid phase, owing to the lower ionization threshold of H_2O in the liquid compared with the gas phase.

We have addressed single pulses in this investigation and acknowledge that after several plasma pulses, the temperature of the liquid surface may increase, which in turn can lead to a higher water vapor density above the surface [58]. The higher water vapor density above the liquid surface could impact our findings in several ways. The higher water vapor density at the surface, coupled with the SIW propagating through this layer, would likely produce higher fluxes of reactive oxygen species (ROS) and near UV radiation (for example, from OH(A)) onto the surface. The reactions which initiate dissociation of PFO^-_{aq} depend weakly on these fluxes. Larger fluxes of H_2O^+ and H_3O^+ relative to, for example, Ar^+ might diminish the contribution of charge exchange to dissociation. Absorption of VUV radiation by the water vapor prior to reaching the liquid surface might impact the contribution of photolysis.

From a more general perspective, this work leads to two primary conclusions. The first is that VUV photons can be important for plasma-liquid reactivity, particularly in argon-containing mixtures, where the VUV photon fluence can exceed the electron fluence by an order of magnitude. VUV photons not only dissociate surfactant molecules, but also generate reactive species in the bulk liquid, such as OH_{aq} and solvated electrons, which can initiate additional chemical pathways. The second conclusion is that the distance between the SIW and the ground electrode plays a fundamental role in reactivity, as demonstrated by the strong dependence of SIW properties on liquid thickness. Engineering the thickness of the liquid when treated by APPs is perhaps an underutilized opportunity.

Acknowledgements This work was supported by the 3M Company, the Army Research Office (W911NF-20-1-0105), the U.S. Department of Energy Office of Fusion Energy Sciences (DE-SC0020232), and the National Science Foundation (CBET-2032604).

Author Contributions T. C. D, J. J., S. O., X. Q, S. M. T and M. J. K collaboratively discussed and developed the scientific principles, intepretations and insights presented in this paper. T. C. D and J. J. performed the simulations. T. C. D. and J. J. wrote the first draft of the manuscript that was critically reviewed and edited by all authors.

Data Availability The data supporting the results discussed in this paper are contained in the paper or available by reasonable request to the authors.

Declarations

Competing interests The authors declare no competing interests.

References

1. Bruggeman PJ, Kushner MJ, Locke BR, Gardeniers JGE, Graham WG, Graves DB, Hofman-Caris RCHM, Maric D, Reid JP, Ceriani E, Fernandez Rivas D, Foster JE, Garrick SC, Gorbanev Y, Hamaguchi S, Iza F, Jablonowski H, Klimova E, Kolb J, Krcma F, Lukes P, Machala Z, Marinov I, Mariotti D, Mededovic Thagard S, Minakata D, Neyts EC, Pawlat J, Petrovic ZL, Pflieger R, Reuter S, Schram DC, Schröter S, Shiraiwa M, Tarabová B, Tsai PA, Verlet JRR, von Woedtke T, Wilson KR, Yasui K, Zvereva G (2016) Plasma Sources Sci Technol 25:053002
2. Kovačević VV, Sretenović GB, Obradović BM, Kuraica MM (2022) J Phys D Appl Phys 55:473002
3. Anderson CE, Cha NR, Lindsay AD, Clark DS, Graves DB (2016) Plasma Chem Plasma Proc 36:1393
4. Locke BR, Thagard SM (2012) Plasma Chem Plasma Proc 32:875
5. Bruggeman PJ, Frontiera RR, Kortshagen UR, Kushner MJ, Linic S, Schatz GC, Andaraarachchi H, Exarhos S, Jones LO, Mueller CM, Rich CC, Xu C, Yue Y, Zhang Y (2021) J Appl Phys 129:200902
6. Bruggeman PJ, Frontiera RR, Kortshagen U, Kushner MJ, Linic S, Schatz GC, Andaraarachchi H, Chaudhuri S, Chen H-T, Clay CD, Dias TC, Doyle S, Jones LO, Meyer M, Mueller CM, Nam JH, Raisanen A, Rich CC, Srivastava T, Xu C, Xu D, Zhang Y (2025) J Chem Phys 162:071001
7. Xu C, Andaraarachchi HP, Kortshagen UR (2024) Nanomaterials 14:1758
8. Nam JH, Bruggeman P (2025) Plasma Proc Polym 22:2400140
9. Chen Q, Li J, Li Y (2015) J Phys D 48:424005
10. Doyle SJ, Dias TC, Meyer M, Kushner MJ (2025) Plasma Sources Sci Technol 34:035004
11. Laroussi M, Bekeschus S, Keidar M, Bogaerts A, Fridman A, Lu X, Ostrikov K, Hori M, Stapelmann K, Miller V, Reuter S, Laux C, Mesbah A, Walsh J, Jiang C, Thagard SM, Tanaka H, Liu D, Yan D, Yusupov M (2022) IEEE Trans Radiat Plasma Med Sci 6:127
12. Stapelmann K, Gershman S, Miller V (2024) J Appl Phys 135:160901
13. Konchekov EM, Gusein-zade N, Burmistrov DE, Kolik LV, Dorokhov AS, Izmailov AYu, Shokri B, Gudkov SV (2023) Int J Mol Sci 24:15093
14. Šimek M, Homola T (2021) Euro Phys J D 75:210
15. Mededovic Thagard S (2025) Curr Opin Green Sustain Chem 53:101023
16. Stratton GR, Bellona CL, Dai F, Holsen TM, Thagard SM (2015) Chem Engr J 273:543
17. Saleem M, Tomei G, Beria M, Marotta E, Paradisi C (2022) Chemosphere 307:135800
18. Singh RK, Multari N, Nau-Hix C, Anderson RH, Richardson SD, Holsen TM, Mededovic Thagard S (2019) Environ Sci Technol 53:11375
19. Biondo O, Tomei G, Saleem M, Sretenović GB, Magarotto M, Marotta E, Paradisi C (2023) Chemosphere 341:139972
20. van Rooij O, Wubs J, Höft H, Sobota A (2024) J Phys D 57:115201
21. Xu H, Liu D, Xia W, Chen C, Wang W, Liu Z, Wang X, Kong MG (2018) Phys Plasmas 25:013520
22. Konina K, Kruszelnicki J, Meyer ME, Kushner MJ (2022) Plasma Sources Sci Technol 31:115001
23. Viegas P, Slikboer E, Bonaventura Z, Guaitella O, Sobota A, Bourdon A (2022) Plasma Sources Sci Technol 31:053001
24. Herrmann A, Margot J, Hamdan A (2024) Plasma Sources Sci Technol 33:125009
25. Herrmann A, Margot J, Hamdan A (2025) Plasma Chem Plasma Proc 45:191
26. Burns DC, Ellis DA, Li H, McMurdo CJ, Webster E (2008) Environ Sci Technol 42:9283
27. Kissa E (2001) Fluorinated surfactants and repellents, 2nd edition. Marcel Dekker, Inc., New York
28. Goss K-U (2008) Environ Sci Technol 42:5032
29. Norberg SA, Johnsen E, Kushner MJ (2015) Plasma Sources Sci Technol 24:035026
30. Delgado HE, Elg DT, Bartels DM, Rumbach P, Go DB (2020) Langmuir 36:1156
31. Naumann A, Alesio J, Poonia M, Bothun GD (2022) J Environ Chem Eng 10:107351
32. Rosen MJ, Kunjappu JT (2012) Surfactants and interfacial phenomena, 4th edition. JohnWiley & Sons, Inc., New Jersey
33. Ji Y, Yan N, Brusseau ML, Guo B, Zheng X, Dai M, Liu H, Li X (2021) Environ Sci Technol 55:10480
34. Costanza J, Arshadi M, Abriola LM, Pennell KD (2019) Environ Sci Technol Lett 6:487

35. Tomei G, Saleem M, Scalvini F, Paradisi C, Marotta E (2026) Plasma Chem Plasma Proc 46:10
36. Vasilev M, Suiter J, Bohl D, Thagard SM (2023) Chem Engr J 473:144833
37. Nau-Hix C, Holsen TM, Mededovic Thagard S (2022) Plasma Proc Polym 19:e2200036
38. Haynes WM (ed) (2014) CRC handbook of chemistry and physics, 95th Edition. CRC Press, Boca Raton
39. Buck RC, Franklin J, Berger U, Conder JM, Cousins IT, de Voogt P, Jensen AA, Kannan K, Mabury SA, van Leeuwen SP (2011) Integr Environ Assess Manag 7:513
40. Van Gaens W, Bogaerts A (2013) J Phys D 46:275201
41. Emmert F, Angermann HH, Dux R, Langhoff H (1988) J Phys D 21:667
42. Tian W, Kushner MJ (2014) J Phys D 47:165201
43. Lietz AM, Kushner MJ (2016) J Phys D 49:425204
44. Meyer M, Nayak G, Bruggeman PJ, Kushner MJ (2023) J Phys D 56:285202
45. Itikawa Y, Mason N (2005) J Phys Chem Ref Data 34:1
46. Gallagher JW, Brion CE, Samson JAR, Langhoff PW (1988) J Phys Chem Ref Data 17:9
47. Sander MU, Luther K, Troe J (1993) Ber Bunsenges Phys Chem 97:953
48. Tian P, Kushner MJ (2015) Plasma Sources Sci Technol 24:034017
49. McCann KJ, Flannery MR (1977) Appl Phys Lett 31:599
50. Dorn H-P, Neuroth R, Hofzumahaus A (1995) J Geophy Res Atmos 100:7397
51. Du J, Huang L, Min Q, Zhu L (2013) Geophys Res Lett 40:4788
52. Sapunar M, Meyer M, Ambalampitiya HB, Kushner MJ, Mašín Z (2024) Phys Chem Chem Phys 26:26037
53. Wiens JP, Miller TM, Ard SG, Viggiano AA, Shuman NS (2022) J Phys Chem A 126:9076
54. Douix S, Dossmann H, Nicol E, Duflot D, Giuliani A (2018) Chem Eur J 24:15572
55. Maza WA, Etz BD, Schutt TC, Chaloux BL, Breslin VM, Pate BB, Shukla MK, Owrutsky JC, Epshteyn A (2022) Environ Sci Technol Lett 9:226
56. Kannari F, Suda A, Obara M, Fujioka T (1983) IEEE J Quantum Electron 19:1587
57. Holstein T (1947) Phys Rev 72:1212
58. Silsby JA, Dickenson A, Walsh JL, Hasan MI (2022) Front Phys 10:1

Authors and Affiliations

Tiago C. Dias[1,5] · Jisu Jeon[2] · Stephen Olson[3] · Xuefei Qiu[4] · Selma Mededovic Thagard[4] · Mark J. Kushner[1]

✉ Mark J. Kushner
mjkush@umich.edu

Tiago C. Dias
t.cunha.dias@tue.nl

Jisu Jeon
jisujeon@umich.edu

Stephen Olson
saolson@mmm.com

Xuefei Qiu
qiu@clarkson.edu

Selma Mededovic Thagard
smededov@clarkson.edu

[1] Department of Electrical Engineering and Computer Science, University of Michigan, Ann Arbor, Michigan 48109-2122, USA

[2] Department of Nuclear Engineering and Radiological Sciences, University of Michigan, Ann Arbor, Michigan 48109-2122, USA

[3] 3M Company, Saint Paul, Minnesota 55144, USA

[4] Department of Chemical and Biomolecular Engineering, Clarkson University, Potsdam, New York 13699, USA

[5] Present address: Department of Applied Physics, Eindhoven University of Technology, Eindhoven, The Netherlands